
Figures and figure supplements

Decoupling global biases and local interactions between cell biological variables

Assaf Zaritsky et al

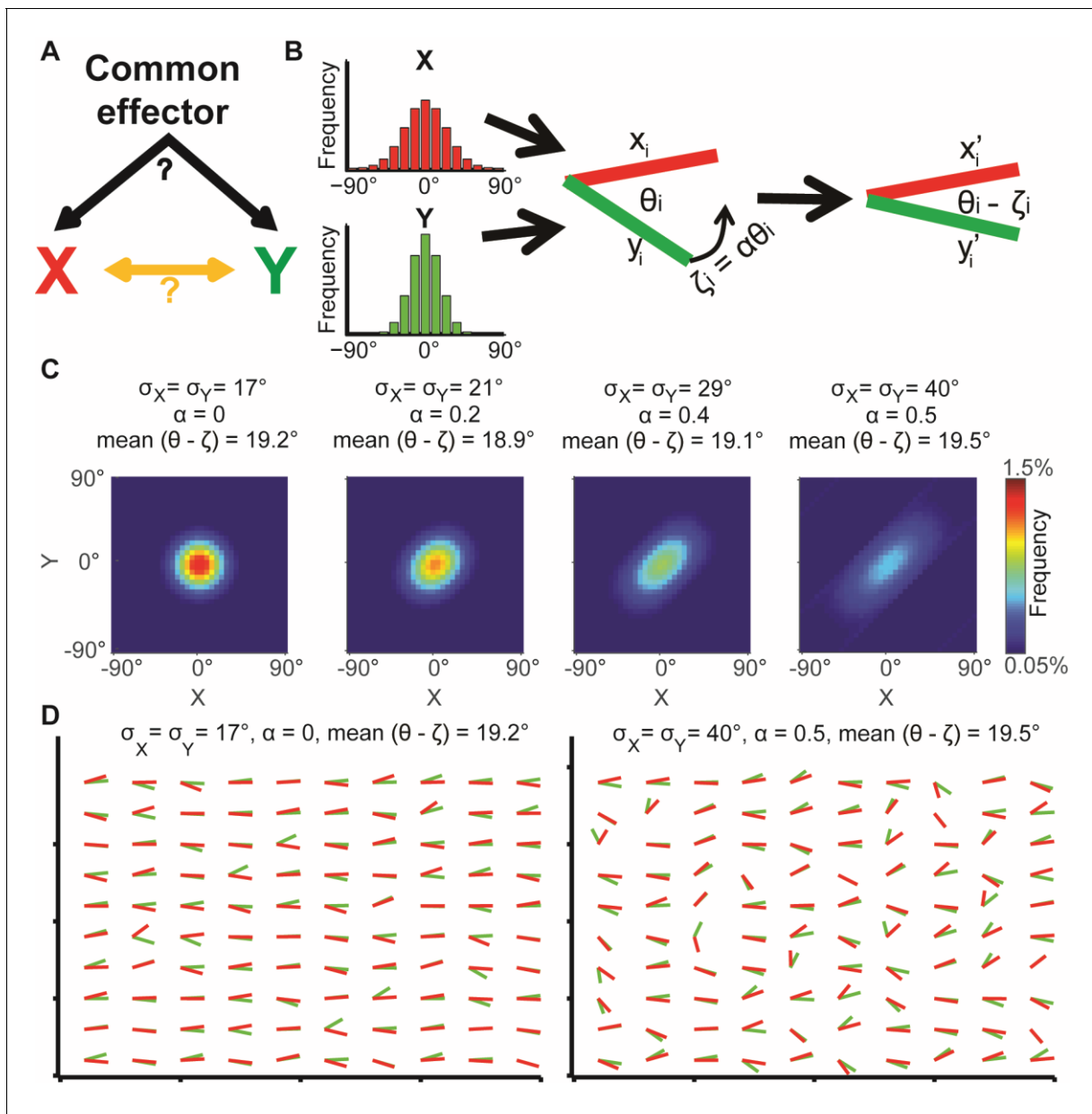
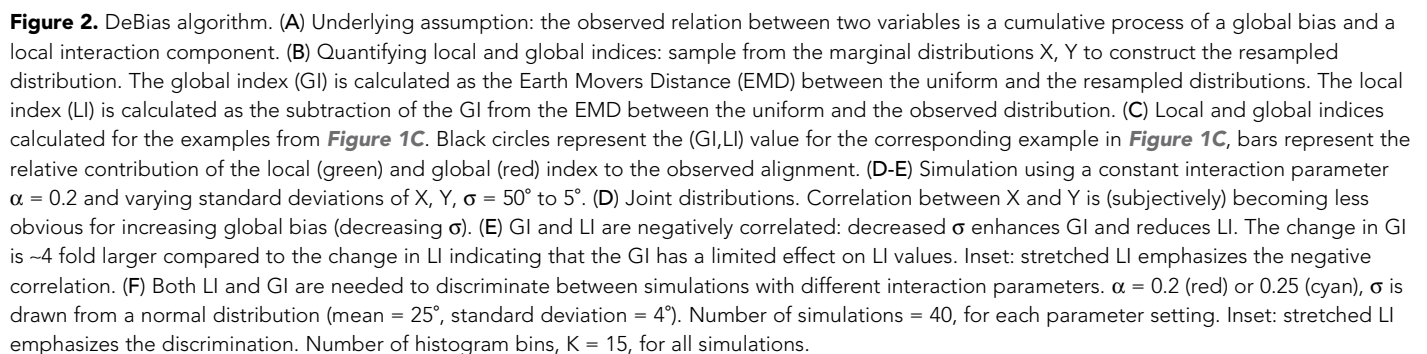


Figure 1. Illustration of global bias and local interaction using the alignment of two orientational variables. (A) The relation between two variables X , Y can be explained from a combination of direct interactions (orange) and a common effector. (B) Simulation. Given two distributions X , Y , pairs of coupled variables are constructed by drawing sample pairs (x_i, y_i) and transforming them to (x'_i, y'_i) by a correction parameter $\zeta_i = \alpha \theta_i$, which represents the effect of a local interaction. α is constant for each of these simulations. (C) Simulated joint distributions. X , Y truncated normal distributions with mean 0 and $\sigma_X = \sigma_Y$. Shown are the joint distributions of 4 simulations with reduced global bias (i.e., increased standard deviation σ_X , σ_Y) and increased local interaction (left-to-right). All scenarios have similar observed mean alignment of $\sim 19^\circ$. (D) Example of 100 draws of coupled orientational variables from the two most extreme scenarios in panel C. Most orientations are aligned with the x-axis when the global bias is high and no local interaction exists (left), while the orientations are less aligned with the x-axis but maintain the mean alignment between (x'_i, y'_i) pairs for reduced global bias and increased local interaction (right).

DOI: [10.7554/eLife.22323.003](https://doi.org/10.7554/eLife.22323.003)



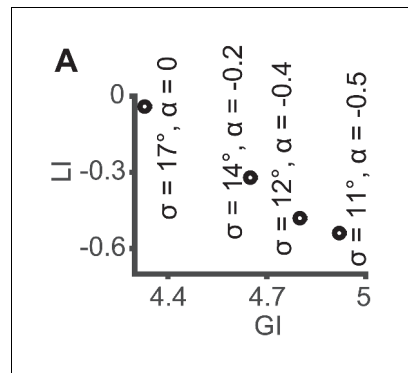


Figure 2—figure supplement 1. Simulations demonstrating the negative local interactions induce negative local indices. Simulations were performed as in **Figure 1B**: X, Y truncated normal distributions with mean 0 and $\sigma = \sigma_X = \sigma_Y$; $\zeta = \alpha\theta$, but with $\alpha < 0$ as the negative interaction. Shown are GI and LI values for four simulations with increased global bias (i.e., smaller standard deviation σ_X, σ_Y) and increased negative local interaction (left-to-right), all scenarios have similar observed mean alignment of $\sim 19^\circ$ (corresponding to the simulations in **Figure 1C**).

DOI: [10.7554/eLife.22323.005](https://doi.org/10.7554/eLife.22323.005)

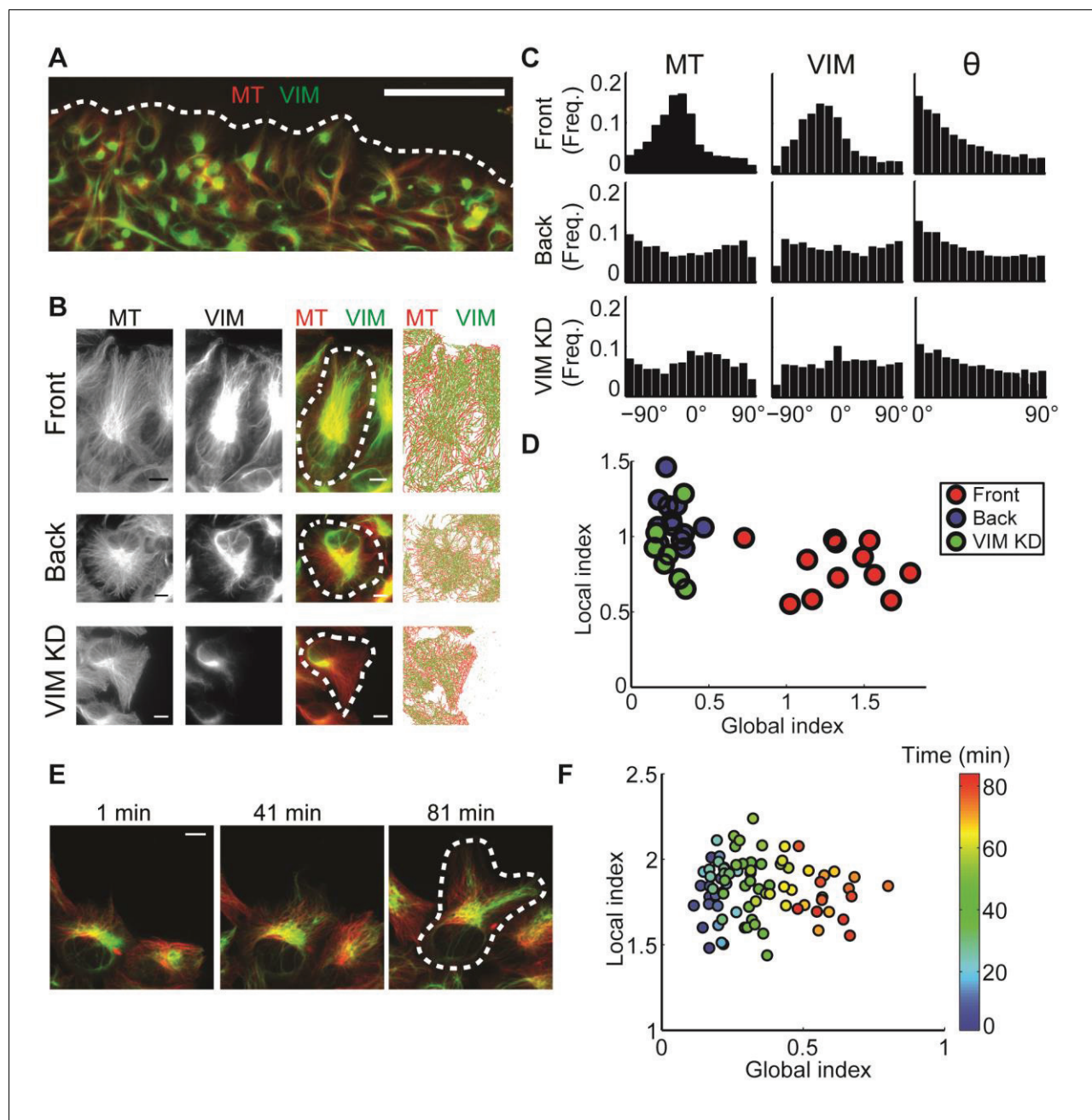


Figure 3. Alignment of microtubule and vimentin intermediate filaments in the context of cell polarity. (A) RPE cells expressing TagRFP α -tubulin (MT) and mEmerald-vimentin (VIM) at endogenous levels during a wound healing assay. Scale bar 100 μ m. (B) Zooming in on cells in different locations in respect to the wound edge. Right-most column, computer segmented filaments of both cytoskeleton systems. Top row, cells located at the wound edge ('Front'); Middle row, cells located 2–3 rows away from the wound edge ('Back'); Bottom row, cells located at the wound edge partially with shRNA knock-down of vimentin. Scale bar 10 μ m. (C) Orientation distribution of microtubules (left column) and vimentin filaments (middle columns) for the cells outlined in B. Vimentin-microtubule alignment distributions (right column). (D) Scatterplot of GI versus LI derived by DeBias. The GI is significantly higher in WT cells at the wound edge ('Front', $n = 12$) compared to cells inside the monolayer ('Back', $n = 12$, fold change = 4.8, p -value < 0.0001); or compared to vimentin-depleted cells at the wound edge ('VIM KD', $n = 7$, fold change = 5.2, p -value < 0.0001). Statistics based on Wilcoxon rank-sum test. All DeBias analyses performed with $K = 15$. (E) Polarization of RPE cells at the wound edge at different time points after scratching. Scale bar 10 μ m. (F) Representative experiment showing the progression of LI and GI as a function of time after scratching (see color code). Correlation between GI and time ~ 0.90 , p -value < 10^{-30} (n time points = 83). $N = 5$ independent experiments were conducted of which four experiments showed a gradual increase in GI with increased observed polarity. All DeBias analyses performed with $K = 15$.

DOI: [10.7554/eLife.22323.006](https://doi.org/10.7554/eLife.22323.006)

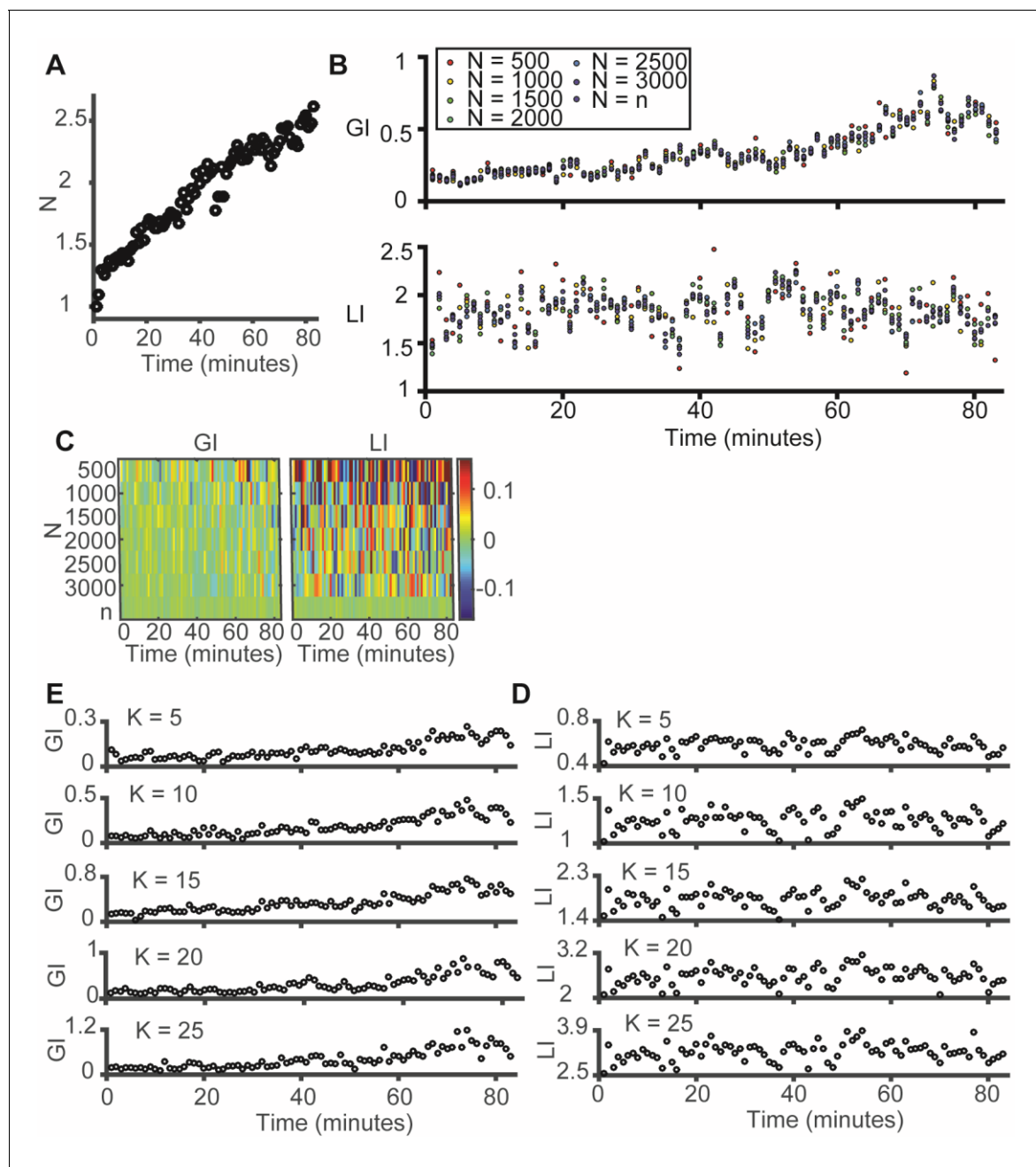


Figure 3—figure supplement 1. LI and GI are independent of the number of observations (N) and the number of histogram bins (K) – experimental evidence from the data in **Figure 3E–F** (time evolution of microtubule-vimentin alignment). (A) Time evolution of N, the number of observations (paired microtubule and vimentin pixels) analyzed, N grows linearly in time. Y-axis was normalized to the first time point. (B–C) LI and GI are independent of the number of random resampled observations $N = 500\text{--}3000$. (B) LI and GI remain stable. (C) Deviation from the LI, GI values reported in **Figure 3F**. Lower N correspond to higher variability. All analyses performed with $K = 15$. (D–E) LI and GI patterns are independent of the number of alignment histogram bins $K = 5\text{--}25$. (D) GI. (E) LI.

DOI: [10.7554/eLife.22323.007](https://doi.org/10.7554/eLife.22323.007)

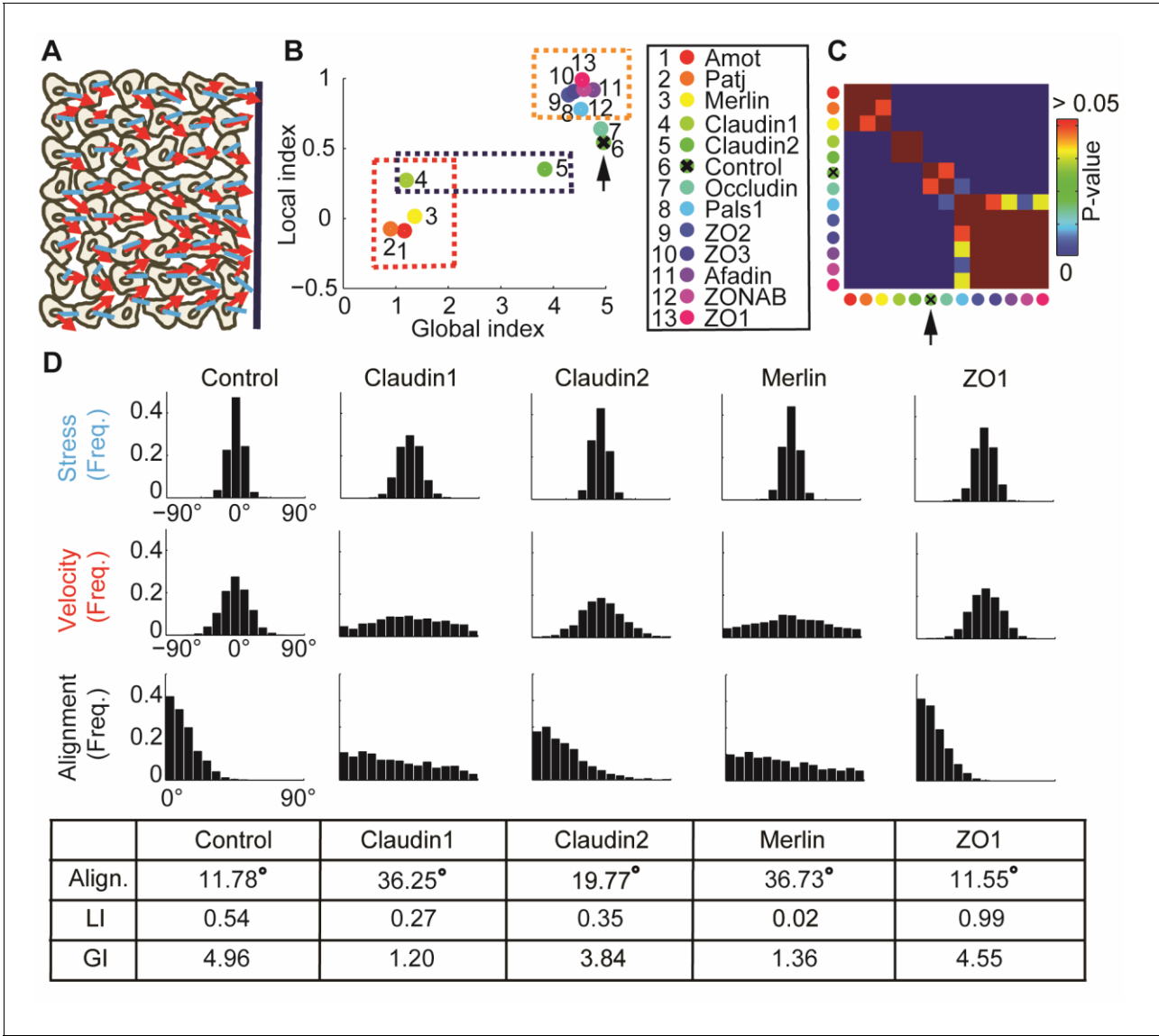


Figure 4. : Alignment of stress orientation and velocity direction during collective cell migration. (A) Assay illustration. Wound healing assay of MDCK cells. Particle image velocimetry was applied to calculate velocity vectors (red) and monolayer stress microscopy to reconstruct stresses (blue). Alignment of velocity direction and stress orientation was assessed. (B) Mini-screen that includes depletion of 11 tight-junction proteins and Merlin. Data from (Das et al., 2015), where effective depletion was demonstrated. Shown are GI and LI values; molecular conditions are sorted by the LI values (control is ranked sixth, pointed by the black arrow). Each dot was calculated from accumulation of 3 independent experiments (N = 925–1539 for each condition). Three groups of tight junction proteins are highlighted by dashed rectangles: red - low LI and GI compared to control, purple – different GI but similar LI, orange – high LI. All DeBias analyses were performed with K = 15. (C) Pair-wise statistical significance for LI values. P-values were calculated via a permutation-test on the velocity and stress data (Materials and methods). Red – no significant ($p \geq 0.05$) change in LI values, blue – highly significant (< 0.01) change in LI values. (D) Highlighted hits: Claudin1, Claudin2, Merlin and ZO1. Top: Distribution of stress orientation (top), velocity direction (middle) and motion-stress alignment (bottom). Bottom: table of mean alignment angle, LI and GI. Claudin1 and Claudin2 have similar mechanisms for transforming stress to aligned velocity. ZO1 depletion enhances alignment of velocity by stress.

DOI: 10.7554/eLife.22323.009

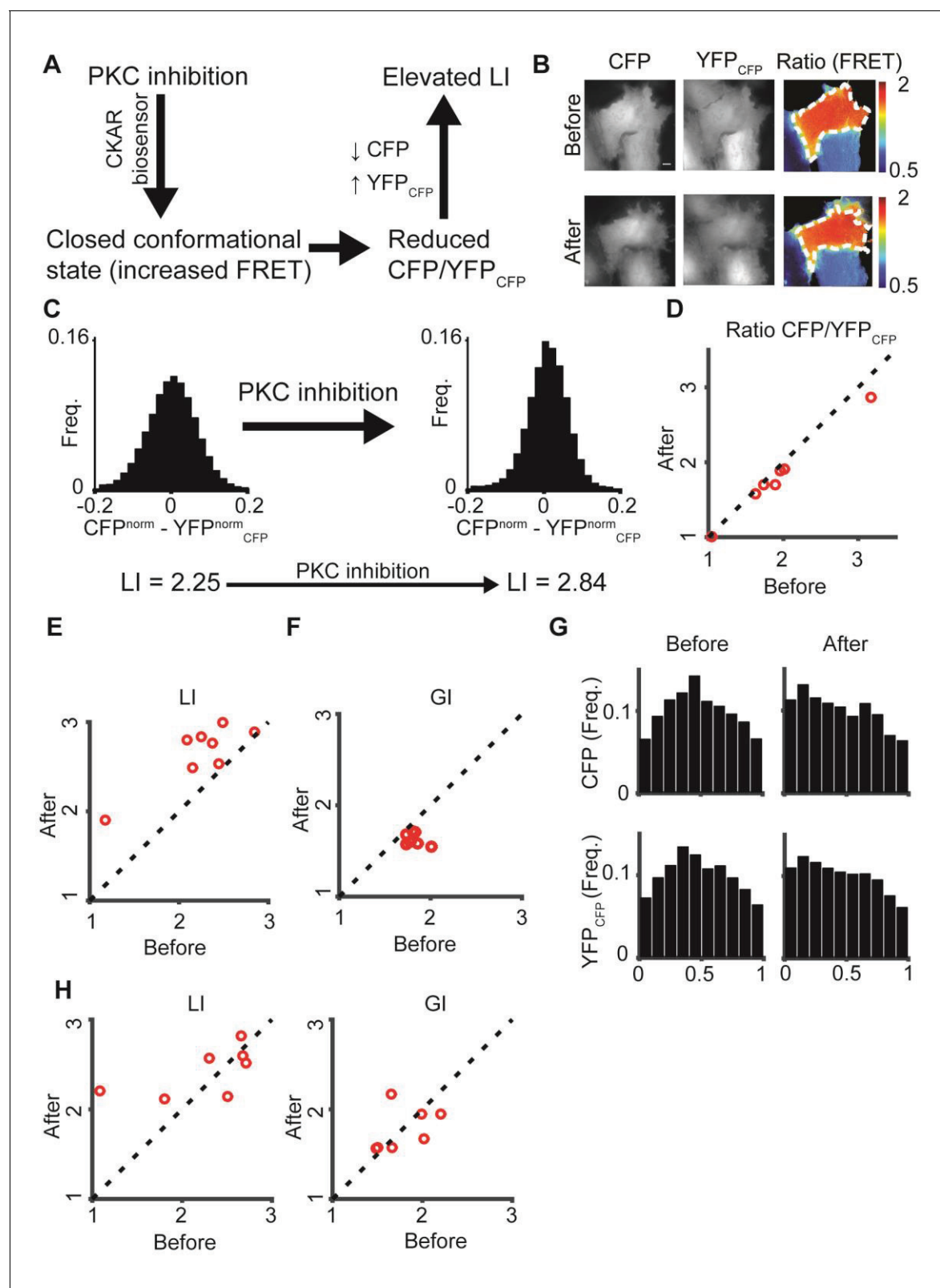


Figure 5. PKC inhibition alters LI and GI. (A) PKC inhibition is expected to lead to elevated LI for cells with dominant CFP signal ($\text{CFP} > \text{YFP}_{\text{CFP}}$). Upon FRET, CFP signal is locally transferred to YFP_{CFP} , reducing the difference in normalized intensity between the two channels, which increases LI. (B) hTERT-RPE-1 cells imaged with the CKAR reporter. A cell before (top) and after (bottom) PKC inhibition. Region of interest was manually annotated and Figure 5 continued on next page

Figure 5 continued

the ratio $\frac{CFP}{YFP_{CFP}}$ was calculated within it. (C) Pixel distribution of differences in normalized fluorescent intensities $CFP^{norm} - YFP^{norm}_{CFP}$ before and after PKC inhibition for the cell from panel B. PKC inhibition shifted the average absolute difference from 0.054 to 0.042 and the LI from 2.25 to 2.84. (D–F) PKC inhibition experiment. N = 8 cells. Statistics based on Wilcoxon sign-rank test. (D) The FRET ratio $\frac{CFP}{YFP_{CFP}}$ decreased (p-value < 0.008), (E) LI increased (p-value < 0.008), and (F) GI decreased (p-value < 0.008) after PKC inhibition. (G) Marginal distribution of CFP and YFP_{CFP} before (top) and after (bottom) PKC inhibition. (H) Control experiment. N = 7 cells. hTERT-RPE-1 cells expressing cytoplasmic GFP and mCherry before and after PKC inhibition. No significant change in LI or GI was observed. All DeBias analyses were performed with K = 19.

DOI: [10.7554/eLife.22323.010](https://doi.org/10.7554/eLife.22323.010)

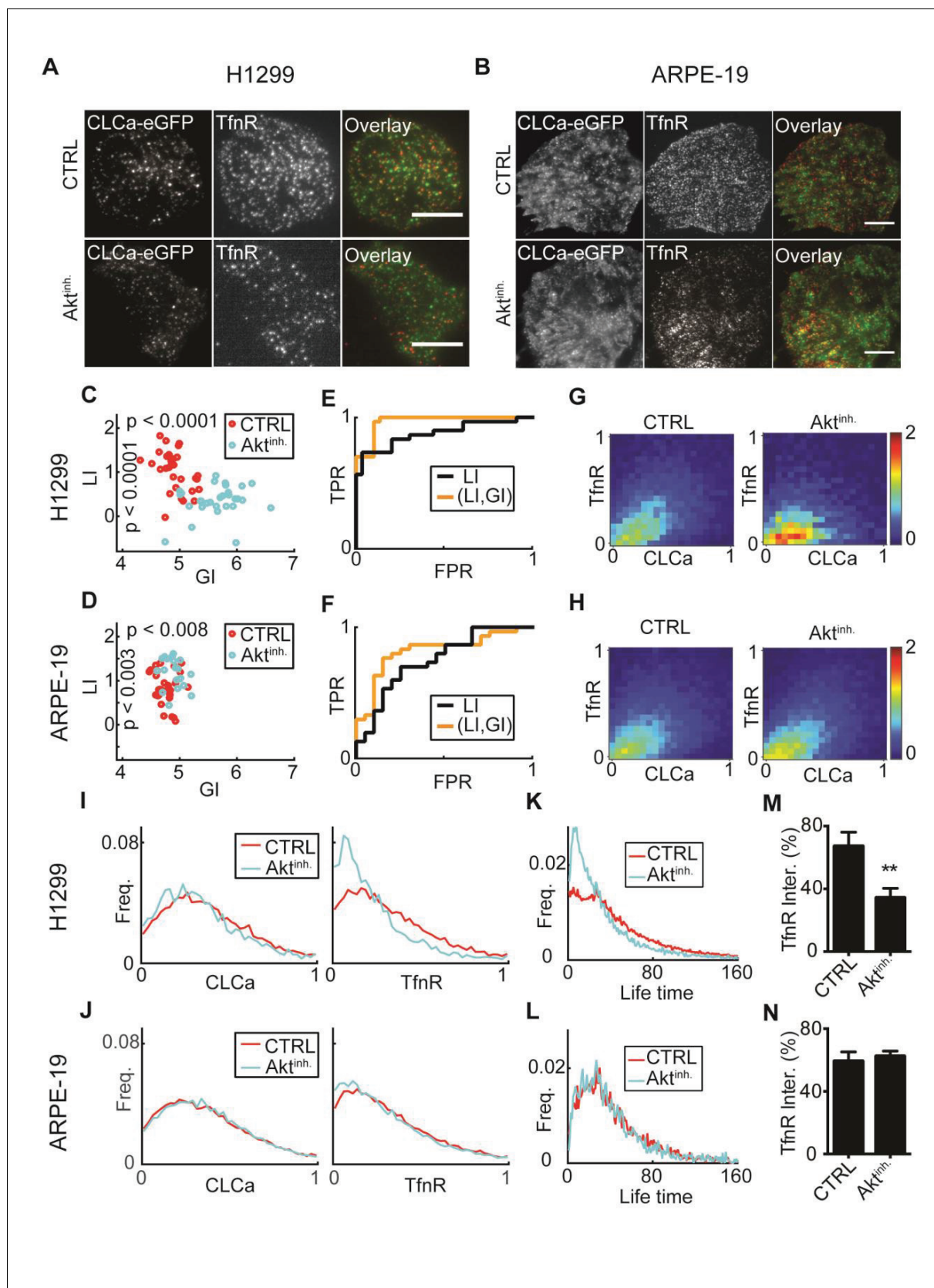


Figure 6. : AKT inhibition differentially alters recruitment of TfnR to CCPs during CME for different cell lines. **(A)** H1299 cells expressing CLCa and TfnR ligands. Top row, representative WT cell (TfnR ligand, GI = 4.6, LI = 1.6). Bottom row, representative AKT-inhibited cell (TfnR ligand, GI = 6.0, LI = 0.3).
 Figure 6 continued on next page

Figure 6 continued

Scale bar 10 μm . (B) ARPE-19 cells. Top row, representative WT cell (TfnR ligand, GI = 4.3, LI = 0.8). Bottom row, representative AKT-inhibited cell (TfnR ligand, GI = 4.6, LI = 1.6). (C–D) LI and GI of CLCa-TfnR co-localization for Ctrl (red) and Akt^{inh.} cells (cyan). Every data point represents the LI and GI values for a single cell. Statistical analyses performed with the Wilcoxon rank-sum test. All DeBias analyses were performed with K = 40. (C) H1299: N number of cells Ctrl = 30, Akt^{inh.} = 30; number of CCPs per cell: Ctrl = 455.5, Akt^{inh.} = 179.5. GI p-value < 0.0001, LI p-value < 0.0001. (D) ARPE-19: N number of cells Ctrl = 30, Akt^{inh.} = 20; number of CCPs per cell: Ctrl = 958.8, Akt^{inh.} = 1138.2. GI p-value < 0.002, LI p-value < 0.008. (E–F) Receiver Operating Characteristic (ROC) curves showing the true positive rates as a function of false-positive rates for single cell classification, higher curves correspond to enhanced discrimination (Materials and methods). Black – LI, orange – (GI,LI). Statistics via permutation test (Materials and methods). (E) H1299 AUC: (GI,LI) = 0.96 versus LI = 0.88, p-value \leq 0.003. (F) ARPE-19 AUC: (GI,LI) = 0.83 versus LI = 0.72, p-value \leq 0.048. (G–H) Joint distributions of CLCa (x-axis) and TfnR (y-axis) for H1299 (G) and ARPE-19 (H) cells. (I–J) Marginal distributions of CLCa (left) and TfnR (right) for H1299 (I) and ARPE-19 (J) cells. (K–L) Combined CCP lifetime distribution for 50 Ctrl (red) and Akt^{inh.} (cyan) cells. Statistics with Wilcoxon rank-sum test (Materials and methods). (K) H1299: p-value < 0.006 (mean EMD: Ctrl = 29.3 versus Akt^{inh.} = 43.6); number of cells: 50 (Ctrl), 11 (Akt^{inh.}). (L) H1299: p-value n.s. (mean EMD: Ctrl = 36.1 versus Akt^{inh.} = 38.0); number of cells: 12 (Ctrl), 12 (Akt^{inh.}). (M–N) Percentage of TfnR uptake: Ctrl versus Akt^{inh.} (whiskers - standard deviation). Statistics via two-tailed Student's t-test. (M) H1299: p-value < 0.005; N = 3 independent experiments. (N) ARPE-19: p-value n.s.; N = 3 independent experiments.

DOI: [10.7554/eLife.22323.011](https://doi.org/10.7554/eLife.22323.011)

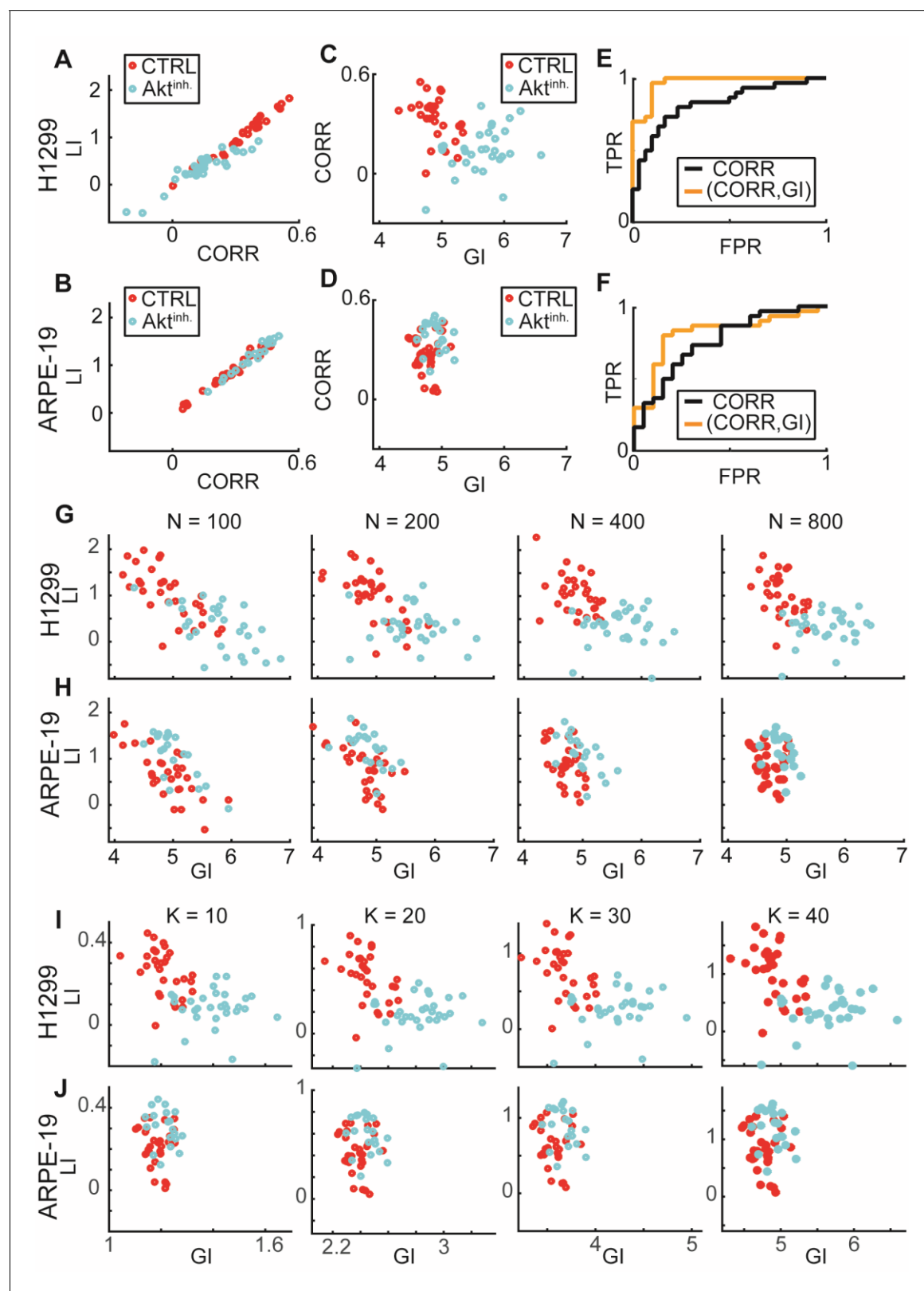
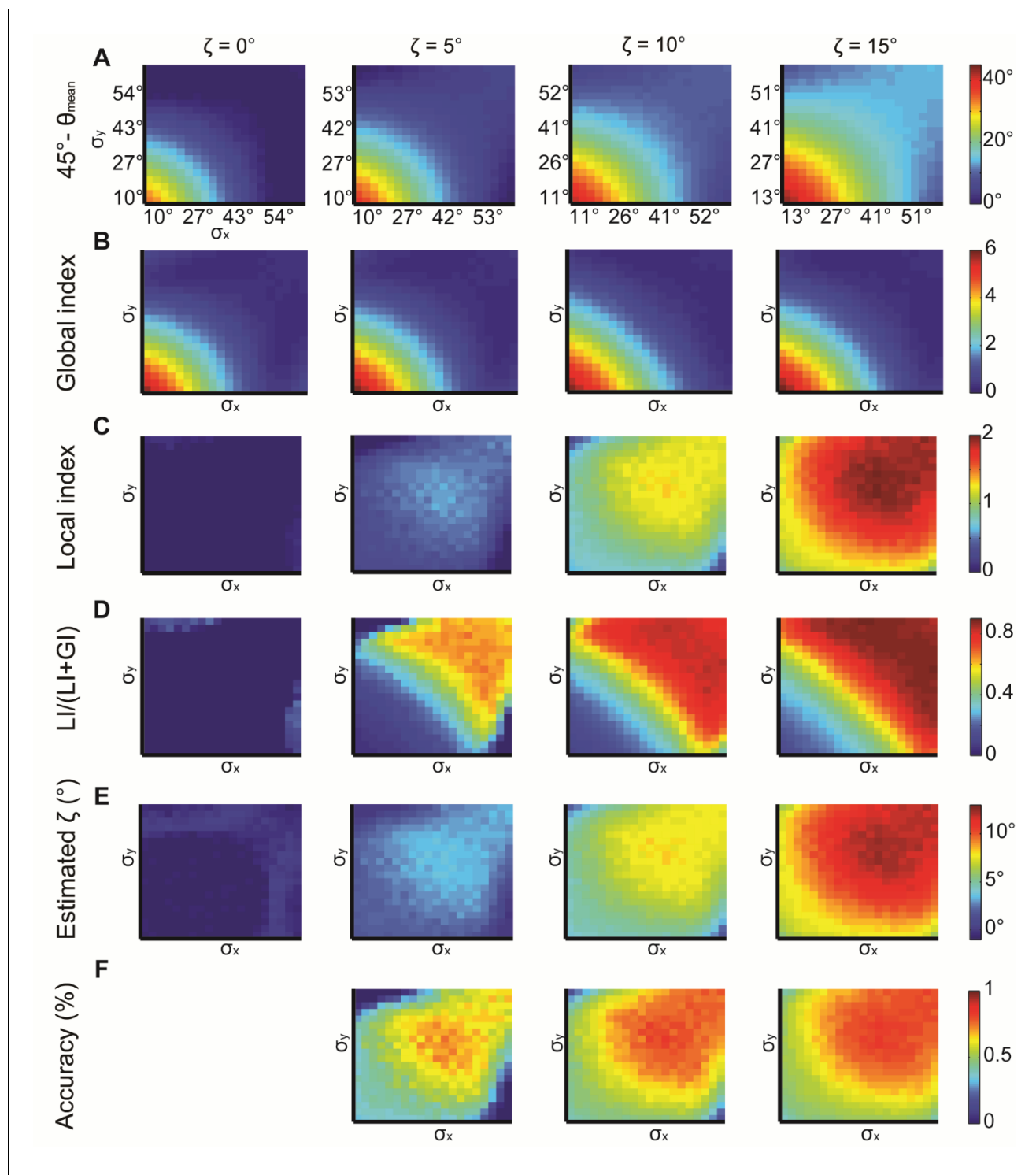


Figure 6—figure supplement 1. : GI encodes information that is distinct from local interactions; Experimental validations of DeBias for co-localization. Data from **Figure 6**. (A–F) GI as a complementary measure. (A–B) LI and Pearson’s correlation (CORR) are highly associated (statistical analyses performed using Pearson’s correlation). (A) H1299 cells: $\rho = 0.95$, p -value $< 10^{-29}$. (B) ARPE-19 cells: $\rho = 0.98$, p -value $< 10^{-32}$. (C–D) CORR vs. GI. Figure 6—figure supplement 1 continued on next page

Figure 6—figure supplement 1 continued

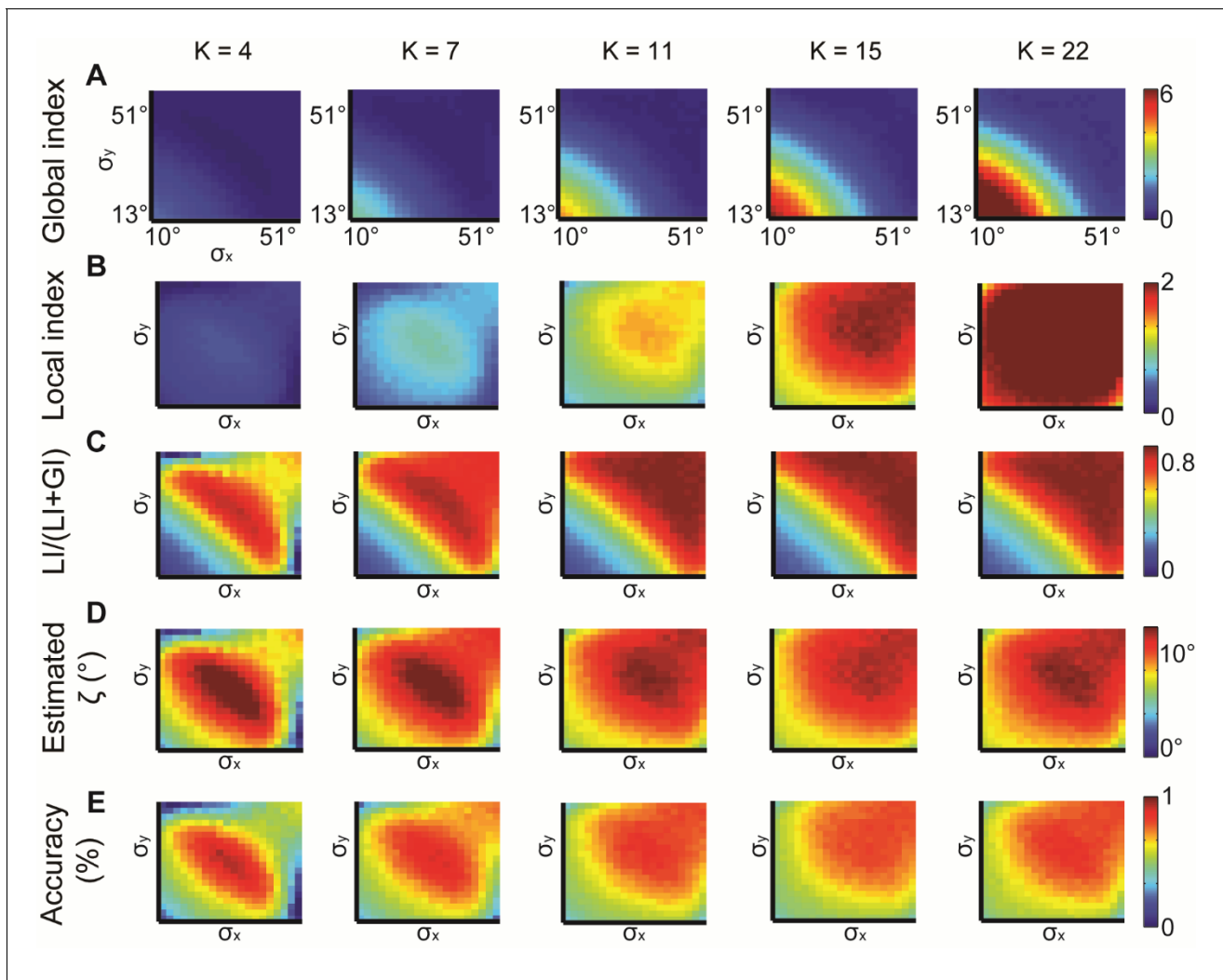
(C) H1299. (D) ARPE-19. (E–F) ROC curves. Statistics via permutation test (Materials and methods). (E) H1299 AUC: (GI,CORR) = 0.96 versus CORR = 0.83, p-value ≤ 0.0001 . (F) ARPE-19 AUC: (GI,CORR) = 0.84 versus CORR = 0.72, p-value n.s.. (G–H) Similar LI, GI values for different number of observations N = 100, 200, 400, 800. (G) H1299. (H) ARPE-19. (I–J) LI and GI patterns are independent of the number of alignment histogram bins K = 10, 20, 30, 40. (I) H1299. (J) ARPE-19.

DOI: [10.7554/eLife.22323.012](https://doi.org/10.7554/eLife.22323.012)



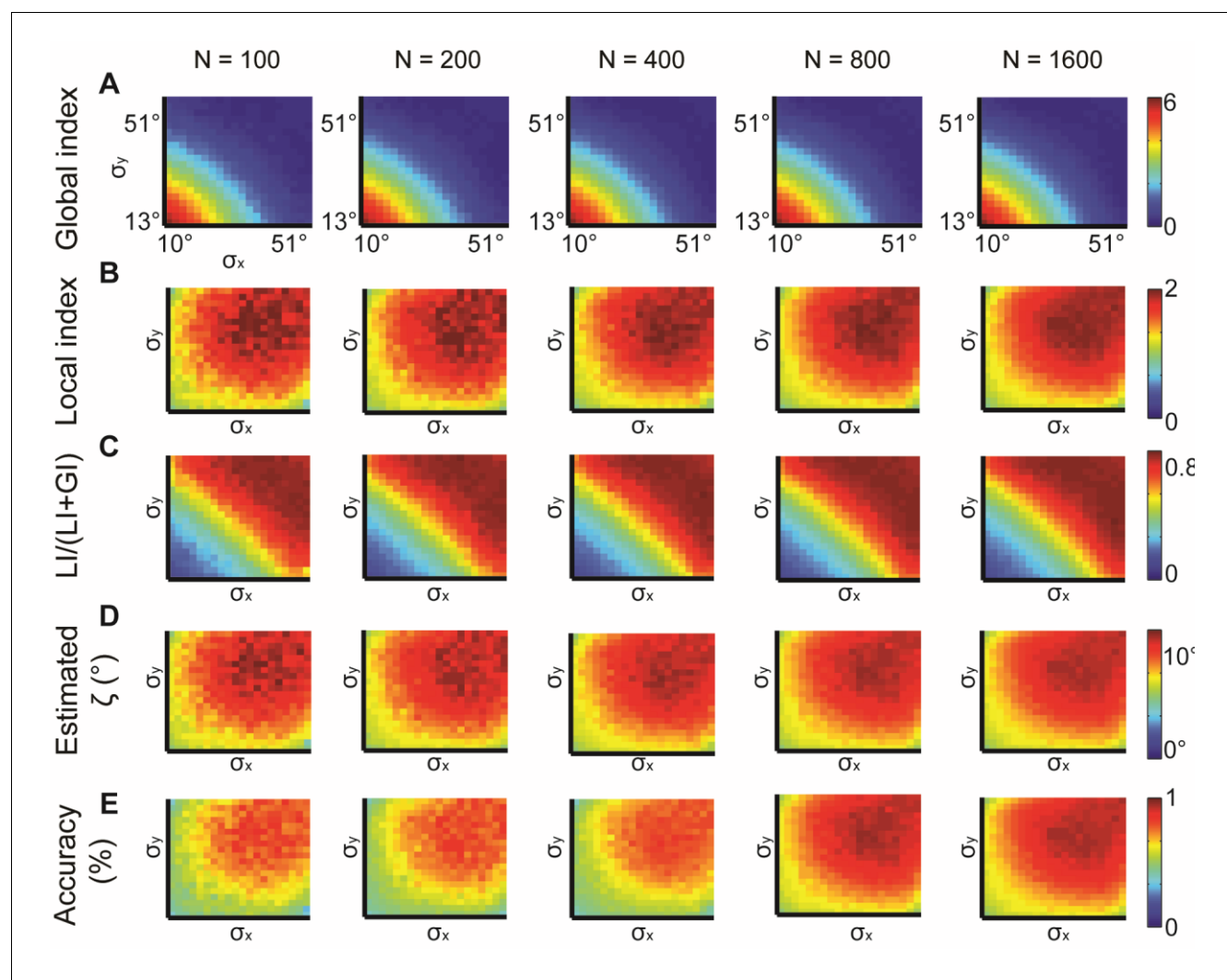
Appendix 2—figure 1. Simulations for X, Y normal distributions with different σ_x , σ_y and constant $\zeta = 0^\circ, 5^\circ, 10^\circ, 15^\circ$. (A) $45^\circ - \theta_{\text{mean}}$ reflecting the cumulative effect of the global bias and the local interaction between X, Y (θ_{mean} is the mean observed alignment). Lower variance and higher ζ correspond to better alignment. (B) Global index. ζ has a small effect on GI. (C) Local index. ζ has a major effect on LI. (D) Relative contribution of LI to the observed alignment increases as function of ζ . (E) Retrieved estimated ζ calculated as the relative contribution of LI to the observed alignment (panel D) times the cumulative effect of the global bias and the local interaction (panel A). (F) Accuracy of estimated ζ grows with ζ and with lower σ_x , σ_y . Note, that this estimation is a lower bound for the true ζ (Appendix 1, Theorem 4). Accuracy cannot be measured for $\zeta = 0^\circ$ hence the empty panel.

DOI: [10.7554/eLife.22323.013](https://doi.org/10.7554/eLife.22323.013)



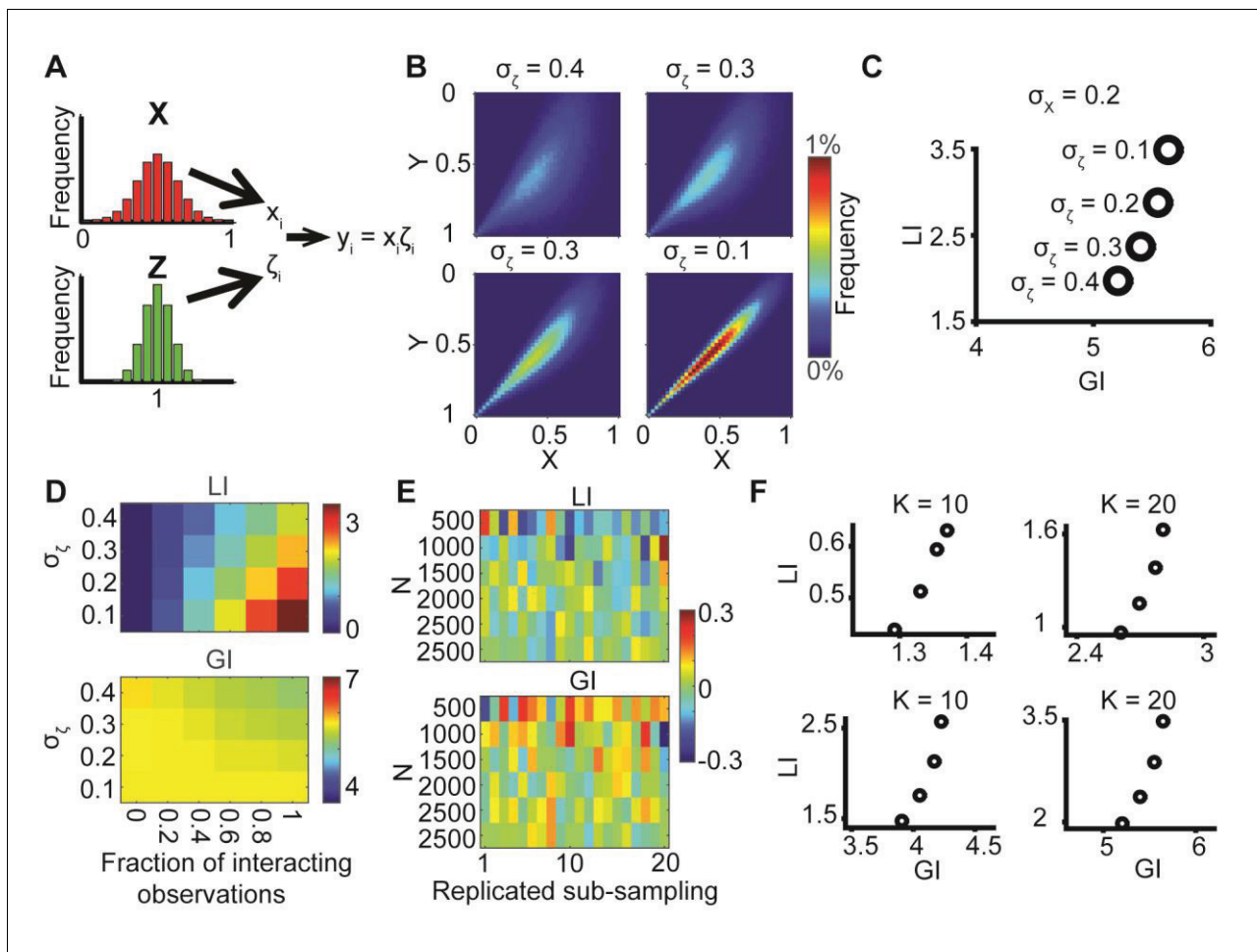
Appendix 2—figure 2. Simulations for different values of K , the number of bins in the alignment distribution. X , Y normal distributions with different σ_x, σ_y and constant $\zeta = 15^\circ$. $K = 4, 7, 11, 15, 22$ were examined. (A–B) Global (A) and local (B) indices grow with K . (C–E) Relative contribution of LI to the observed alignment (C), Retrieved estimated ζ (D) and accuracy of estimated ζ (E) stabilizes for $K \geq 11$.

DOI: [10.7554/eLife.22323.014](https://doi.org/10.7554/eLife.22323.014)



Appendix 2—figure 3. Simulations for different N , the number of observations. $N = 100, 200, 400, 800, 1600$ were examined. X, Y normal distributions with different σ_x, σ_y and constant $\zeta = 15^\circ$. All measures provide similar information but are noisier for lower N . (A) Global index. (B) Local index. (C) Relative contribution of LI to the observed alignment. (D) Retrieved estimated ζ . (E) Accuracy of estimated ζ .

DOI: [10.7554/eLife.22323.015](https://doi.org/10.7554/eLife.22323.015)



Appendix 3—figure 1. Simulating co-localization. (A) Simulation. We use the distributions $X = N(\mu_x = 0.5, \sigma_x)$, $Z = N(\mu_z = 1, \sigma_z)$, where X is truncated to $[0, 1]$. Pairs of coupled variables are constructed by drawing sample pairs (x_i, ζ_i) and constructing $y_i = x_i \zeta_i$ (Materials and methods). (B) Simulated joint distributions. Shown are the joint distributions of 4 simulations with increased global bias (i.e., decreased μ_z). (C) Local and global indices calculated for the examples from panel B. Smaller ζ_i associate with larger LI. The weaker negative association between GI and σ_z is because larger σ_z induces a distribution Y that is more spread compared to X which reduces the GI. (D) Simulations of partial co-localization. A given fraction of observations for Y were calculated as shown in panels A–C, the rest were independently drawn from the distribution X implying no local interaction. Shown are LI (top) and GI (bottom) as functions of the fraction of locally interacting observations and σ_z . LI associates with increased fraction of locally-interacting observations, whereas the effect is minor in GI, in accordance with panel C. (E) Deviation of LI, GI values reported in panel C as functions of the number of observations n . 20 independent sub-sampling. Lower n associates with higher variability. No other trend is observed. (F) LI and GI patterns are independent of the number of alignment histogram bins $K = 10$ –40. Equal size of dynamic ranges was set for LI and GI plots in panels C, D and F. K , number of histogram bins was set to 40 for all panels excluding F. $\sigma_x = 0.2$ for panels B–E.

DOI: [10.7554/eLife.22323.016](https://doi.org/10.7554/eLife.22323.016)